



HAL
open science

Fate of Springtime Atmospheric Reactive Mercury: Concentrations and Deposition at Zeppelin, Svalbard

Stefan Osterwalder, Sarrah Dunham-Cheatham, Beatriz Ferreira Araujo, Olivier Magand, Jennie Thomas, Foteini Baladima, Katrine Aspmo Pfaffhuber, Torunn Berg, Lei Zhang, Jiaoyan Huang, et al.

► **To cite this version:**

Stefan Osterwalder, Sarrah Dunham-Cheatham, Beatriz Ferreira Araujo, Olivier Magand, Jennie Thomas, et al.. Fate of Springtime Atmospheric Reactive Mercury: Concentrations and Deposition at Zeppelin, Svalbard. ACS Earth and Space Chemistry, 2021, 5 (11), pp.3234-3246. <10.1021/acsearthspacechem.1c00299>. <hal-04482777>

HAL Id: hal-04482777

<https://hal.univ-grenoble-alpes.fr/hal-04482777v1>

Submitted on 4 Apr 2024

HAL is a multi-disciplinary open access archive for the deposit and dissemination of scientific research documents, whether they are published or not. The documents may come from teaching and research institutions in France or abroad, or from public or private research centers.

L'archive ouverte pluridisciplinaire HAL, est destinée au dépôt et à la diffusion de documents scientifiques de niveau recherche, publiés ou non, émanant des établissements d'enseignement et de recherche français ou étrangers, des laboratoires publics ou privés.




Distributed under a Creative Commons CC BY-SA 4.0 - Attribution - ShareAlike - International License

Fate of Springtime Atmospheric Reactive Mercury: Concentrations and Deposition at Zeppelin, Svalbard

Journal Article

Author(s):

Osterwalder, Stefan ; Dunham-Cheatham, Sarah M.; Ferreira Araujo, Beatriz; Magand, Olivier; Thomas, Jennie L.; Baladima, Foteini; Pfaffhuber, Katrine Aspmo; Berg, Torunn; Zhang, Lei; Huang, Jiaoyan; Dommergue, Aurélien; Sonke, Jeroen E.; Sexauer Gustin, Mae

Publication date:

2021-11-18

Permanent link:

<https://doi.org/10.3929/ethz-b-000512564>

Rights / license:

[In Copyright - Non-Commercial Use Permitted](#)

Originally published in:

ACS Earth and Space Chemistry 5(11), <https://doi.org/10.1021/acsearthspacechem.1c00299>

Fate of springtime atmospheric reactive mercury: Concentrations and deposition at Zeppelin, Svalbard

Stefan Osterwalder^{1,2*}, Sarah M. Dunham-Cheatham³, Beatriz Ferreira Araujo⁴, Olivier Magand¹, Jennie L. Thomas¹, Foteini Baladima¹, Katrine Aspmo Pfaffhuber⁵, Torunn Berg⁶, Lei Zhang⁷, Jiaoyan Huang⁸, Aurélien Dommergue¹, Jeroen E. Sonke⁴, Mae Sexauer Gustin³

¹ Institut des Géosciences de l'Environnement, Université Grenoble Alpes, CNRS, IRD, Grenoble INP, 460 Rue de la piscine, 38400 Saint-Martin-d'Hères, France

² Institute of Agricultural Sciences, ETH Zurich, Universitätsstrasse 2, 8092 Zurich, Switzerland

³ Department of Natural Resources and Environmental Sciences, University of Nevada, 1664 N. Virginia Street Reno, NV 89557, USA

⁴ CNRS, IRD, CET, Université Paul Sabatier–Toulouse III, Observatoire Midi-Pyrénées 14, avenue Édouard Belin 31400 Toulouse, France

⁵ Norwegian Institute for Air Research, Instituttveien 18, 2007 Kjeller, Norway.

⁶ Department of Chemistry, Norwegian University of Science and Technology, Gløshaugen, 7491 Trondheim, Norway

⁷ School of the Environment, Nanjing University, 163 Xianlin Avenue, Nanjing, Jiangsu 210023, China

⁸ Sonoma Technology, 1450 N. McDowell Blvd., Suite 200, Petaluma, California 94954, USA

*corresponding author: stefan.osterwalder@usys.ethz.ch

KEYWORDS:

Aerohead, Arctic, Pollution, RMAS, Speciation, Thermal desorption

1 **Abstract**

2 Mid-latitude atmospheric elemental mercury (Hg) emissions undergo extensive oxidation to reactive
3 Hg (RM) compounds during Arctic polar sunrise, resulting in enhanced atmospheric deposition that
4 impacts Arctic marine wildlife and humans. It has been difficult to estimate RM dry deposition,
5 because RM concentrations, compounds, and their deposition velocities are ill-defined. Here we
6 investigate RM concentrations sampled with membrane-based methods, and find these to exceed
7 denuder-based RM detection by 5 times at the Zeppelin Observatory on Svalbard (March 26 – July 24,
8 2019). Measured dry deposition of GOM was about half of modeled RM deposition demonstrating
9 that particulate-bound Hg was an important component of dry deposition. Using thermal membrane
10 desorption RM chemistry was found to be dominated by Hg–Cl/Br (51%) and Hg–N (45%)
11 compounds. Back trajectory analysis indicated that Hg–Br/Cl compounds were predominantly
12 advected from within the marine boundary layer (sea ice exposure), while Hg–N originated from the
13 free troposphere. Weekly average RM compound-specific dry deposition velocities ranged from 0.12
14 to 0.49 cm s⁻¹, with a net RM dry deposition of 1.9 μg m⁻² (1.5 – 2.5 μg m⁻²; 95% confidence interval),
15 that exceeds the mean annual Hg wet deposition flux in Svalbard. Overall, we find that springtime
16 atmospheric RM deposition has been underestimated in the Arctic marine environment.

SYNOPSIS:

Atmospheric reactive mercury measurements at Svalbard demonstrate elevated deposition to Arctic ecosystems (5.6-times), and input of Hg-N and halogenated compounds.

17 1. Introduction

18 Mercury (Hg) pollution in the Arctic is of concern, because indigenous people rely heavily on marine-
19 based diets that expose them to neurotoxic methylmercury^{1,2}. Globally, the toxic burden of
20 anthropogenic Hg pollution for human and ecosystem health is accepted by policy makers, and has
21 resulted in the UNEP Minamata Convention that aims to reduce human and ecosystem exposure to
22 Hg³. However, to evaluate the effectiveness of the Convention we must improve our understanding on
23 how Hg cycles between air, land, water, ice, and snow, especially in vulnerable ecosystems, such as
24 the Arctic⁴. The uncertainty in estimates of atmospheric Hg deposition as gaseous elemental Hg
25 (GEM), gaseous oxidized Hg (GOM), or as particulate-bound Hg (PBM) to the Arctic Ocean is
26 illustrated by a comparison of two global numerical Hg models. The GEOS-Chem model⁴ suggested
27 an atmospheric Hg input to the Arctic Ocean of 76 Mg yr⁻¹, while the GRAHM model estimated 108
28 Mg yr⁻¹⁵.

29 The discovery of coastal springtime atmospheric Hg depletion events (AMDEs) in 1995 indicated that
30 reactive Hg (RM = GOM + PBM) dry deposition was an important pathway for atmospheric Hg inputs
31 to Arctic marine ecosystems⁶. Subsequent studies suggested that during AMDEs about 100 Mg RM yr⁻¹
32 ¹ was deposited to Arctic snow and ice^{7,8}. Oxidation of GEM to GOM during AMDEs is primarily
33 induced by photochemical activation of sea ice-derived halogen compounds^{8,9}. In particular, bromine
34 oxide and atomic bromine radicals (BrOx, BrO, Br•) lead to the destruction of ozone (O₃) and
35 oxidation of GEM, with subsequent depletion of both GEM and O₃ in the Arctic atmosphere during
36 polar sunrise^{10,11}. Most recently, Obrist et al.¹² found that RM dry deposition to coastal Arctic tundra
37 was substantial during springtime AMDEs, depositing 0.8 – 2.8 µg m⁻² yr⁻¹. Dry deposition of RM
38 during AMDEs results in higher total Hg concentrations in snow^{13,14} that can be followed by re-
39 emission of Hg⁰ after photo-reduction^{2,15,16}. Approximately 90% of the total Hg in snow can be re-
40 emitted back to the atmosphere after AMDEs¹.

41 To assess the total input of Hg to Arctic ecosystems during AMDEs, it is crucial to improve RM dry
42 deposition estimates. This could be done by measuring ambient RM concentrations and applying the
43 values in dry deposition models or identifying RM compounds in ambient air and applying compound-
44 specific deposition velocity calculations based on local meteorological data. The spatial resolution of
45 Arctic RM measurements is limited, and the widely used measurement technique to quantify
46 atmospheric Hg (Tekran® speciation system [Tekran® 2537/1130/1135]; Tekran® Instrument Corp.,
47 Ontario, Canada) has been demonstrated to underestimate RM by a factor of 2 to 13 in the planetary
48 boundary layer¹⁷⁻²⁴, and by a factor of 1.6 in the free troposphere²⁵. Other studies suggest measurement
49 artefacts for PBM are generated by temperature and collection time²⁶⁻²⁸. Selective collection and
50 analysis of particles smaller than 2.5 µm diameter with the Tekran® also raises the question of the
51 possible underestimation of PBM concentrations²⁹ particularly in oceanic environments where the RM
52 compounds are dominantly associated with larger (2 – 10 µm) marine aerosols^{30,31}.

53 The University of Nevada, Reno – Reactive Mercury Active System 2.0 (RMAS), with cation
54 exchange membranes (CEM) and nylon membranes³², in combination with a down-facing
55 aerodynamic sampler housing that also uses CEMs (Aerohead sampler)^{33,34}, have been shown to
56 improve RM concentration measurements, and GOM and RM dry deposition estimates, respectively,
57 relative to the Tekran® 2537/1130/1135 system³⁵. These measurement methods have never been
58 applied in the Arctic, though they are necessary since a low bias in RM deposition would lead to
59 underestimation of Hg transfer from the atmosphere to marine and terrestrial ecosystems during
60 AMDEs. Using the RMAS, the chemistry of RM compounds can be suggested using thermal
61 desorption of nylon membranes and subsequent peak deconvolution^{20,21,32,36}. This methodology allows
62 for understanding if specific compounds namely HgO, Hg-Br/Cl (e.g. HgBr₂, HgCl₂), Hg-nitrogen
63 (e.g., Hg(NO₃)₂), and Hg-sulfur (e.g., HgSO₄), as well as some organic-bound compounds (e.g.,
64 MeHg)²⁴ are present. Knowledge about the chemistry of RM improved local estimates of RM
65 deposition at a coastal research site in Florida, USA³⁶. Estimates of dry deposition were based on
66 compound-specific deposition velocity calculations using a multiple resistance model that was
67 developed by Zhang et al.³⁷ and modified by Lyman et al.³³.

68 Explaining the bias in atmospheric RM concentration among different measurement methods, in
69 combination with better identification of chemical compounds of RM, has been identified as a top
70 priority task to improve the determination of RM dry deposition from local to global scales¹⁸. Here we
71 present a procedure to determine RM compound-specific dry deposition velocities in order to calculate
72 springtime RM dry deposition in the Ny-Ålesund area on Svalbard. The goals of the study were to: 1)
73 intercompare RM concentrations using automated (Tekran®) and manual methods (RMAS); 2)
74 identify RM compounds by thermal desorption procedures; 3) investigate the source of RM
75 compounds using back-trajectory analysis; and 4) calculate RM compound-specific dry deposition
76 velocities and compare them with dry deposition measurements made by the Aerohead sampler. The
77 incorporation of new observations of RM concentration, chemistry and compound-specific dry
78 deposition velocities is a necessary intermediate step toward substantially improving numerical
79 models of Hg cycling in the Arctic.

80 **2. Material and Methods**

81 **2.1 Location and sampling**

82 Air measurements were carried out from March 26 (11:00) to July 24 (08:00), 2019 at the Zeppelin
83 Observatory (Zeppelin), located on Svalbard in the Norwegian Arctic. The atmospheric research and
84 monitoring station was located on Zeppelin Mountain at 474 m a.s.l. (78.90°N, 11.88°E). The
85 observatory was situated far from major air pollution sources, and thus, was within an undisturbed
86 Arctic environment. A steep downhill slope faced north towards the research village of Ny-Ålesund, a
87 small settlement with 35 to 185 inhabitants at 2 km from the sampling site. The station was operated
88 by the Norwegian Institute for Air Research (NILU) in close collaboration with the Norwegian Polar
89 Institute (NPI). Air inlets for all air Hg measurements were installed 3 m above ground in close
90 proximity to one another, facing downward and toward the predominant wind direction (ESE).
91 Automated atmospheric Hg measurements were carried out by Norwegian University of Science and
92 Technology (NTNU) in collaboration with NILU; manual sampling for RM analyzes was performed
93 by NPI staff. Previous analysis of automated atmospheric Hg and snow Hg measurements at Zeppelin
94 were reported by Dommergue et al.¹³, Berg et al.³⁸⁻⁴⁰, Aspino et al.⁴¹, Gauchard et al.⁴², Sprovieri et
95 al.^{43,44}, Sommar et al.⁴⁵, Ferrari et al.⁴⁶, Steen et al.⁴⁷, and Angot et al.⁴⁸.

96 **2.2 Automated GEM and RM measurements**

97 During the campaign, a Tekran® measured GEM, GOM, and PBM continuously following methods
98 briefly described in section S1 and detailed in Landis et al.⁴⁹. The only deviation from the standard
99 operation procedures^{50,51} was calculating GOM with the flush blank concentrations added to the GOM
100 measurement; this was done because adding the Tekran® flush blank to RM (GOM + PBM)
101 measurements resulted in a good agreement with manual RM measurements using polyethersulfone
102 membranes at the high altitude Pic du Midi Observatory²⁵.

103 **2.3 Manual RM measurements**

104 Three different sorption surface materials were used to sample RM. Polyethersulfone membrane (PES,
105 47 mm diameter, 0.45 µm pore size; Millipore) were previously applied^{25,52} and showed a similar
106 sorption capacity and background Hg contents to CEM⁵³. The PES and CEM (PES backbone that has
107 been proprietarily treated, 47 mm diameter, 0.8 µm pore size; Mustang-S, Pall Corporation) were
108 applied extensively in recent studies (e.g., Gustin et al.¹⁹; Maruszczak et al.²⁵; Luippold et al.³², Miller
109 et al.⁵⁴) and were deemed the preferable material for quantitative RM measurements due to the high
110 RM sorption efficiency⁵³. Nylon membranes (47 mm diameter, 0.2 µm pore size; Sartorius Stedium)
111 were used to determine the chemistry of RM using thermal desorption procedures^{19,24}. The chemistry
112 of the RM compounds captured on the nylon membranes was determined by comparing membrane Hg
113 desorption profiles from Svalbard with those developed for standard Hg compounds (see section 2.4
114 also).

115 **2.3.1 PES measurements**

116 The PES sampling configuration captured RM in ambient air by pumping at 1 L min^{-1} (Membrane
117 vacuum pump, KNF) through a one-stage outdoor filter pack protected from snow fall. The airflow
118 was regulated by a ball flow meter (Fisher Scientific) and quantified with a digital volume meter
119 (Siargo Ltd.). The flow was regularly checked with a Bios Defender calibration unit and considered
120 stable throughout the campaign. In the laboratory, the RM content on the PES after digestion was
121 determined using a Brooks Rand Model III cold vapor atomic fluorescence spectrometer (CVAFS).
122 The method detection limit (MDL) was 5 pg Hg^{25} . Details on RM analysis are described in section S2
123 and a data overview is given in section S3. In total, eight blank membranes were collected from the
124 jars that housed the PES prior to deployment of the new samples. The mean Hg content on PES blanks
125 was $13 \pm 8 \text{ pg}$ (1σ , $n = 8$). The limit of detection (LOD) was 25 pg (3σ of blank). The lowest RM on
126 PES was 333 pg , collected from June 4 to June 11, 2019. The blank percentage compared to the
127 median RM was 2% (ranged from 1% to 6%) and all samples were above the LOD.

128 **2.3.2 RMAS membrane total Hg measurements**

129 The RMAS was used to collect RM on CEM and nylon membranes. The sampling procedures for
130 CEM and nylon membranes and their blank treatments were identical. Previous studies showed that
131 nylon membranes did not collect all ambient compounds with the same efficiency as CEMs^{19,53}, but
132 that the RM chemistry was in good agreement with measurements of anions (e.g., Cl^- , Br^- , NO_3^-)²⁴, and
133 that RM compounds sorbed to the membrane did not transform during storage and shipment⁵³. For RM
134 sampling, ambient air was drawn through 6 sampling ports ($n = 3$ CEM, $n = 3$ nylon) at a flow rate of
135 $1.7 \pm 0.2 \text{ L min}^{-1}$. The downstream membranes in the two-stage filter holders allowed for the capture
136 of Hg that passed through the upstream membrane. A detailed description of the RMAS can be found
137 in Luippold et al.²⁴. Triplicate blank CEM and nylon membranes were collected from the same jars as
138 those that held the sample membranes. CEM and downstream nylon membranes were digested and
139 analyzed using CVAFS following EPA Method 1631, and upstream nylon membranes are thermally
140 desorbed (sections 2.4, S2). The mean of the triplicate CEM blanks, collected weekly at the start of
141 each deployment, was $38 \pm 13 \text{ pg}$ (1σ , $n = 17$), and the mean nylon membrane blank Hg content was
142 $14 \pm 7 \text{ pg}$ (1σ , $n = 17$). All CEM samples were above the LOD of 38 pg (3σ of blank); the LOD was
143 less than 5% of the median RM (785 pg). Median CEM breakthrough for all samples was 8% ($n = 17$).
144 The nylon membrane LOD was 20 pg (3σ of blank); the two last samples of the campaign (harvested
145 on July 17 and 24, 2019) were below the LOD. The mean breakthrough on the nylon membrane was
146 2% (1σ , $n = 15$), excluding the samples below the LOD.

147 **2.4 RM compounds**

148 Upstream nylon membranes were thermally desorbed to characterize and quantify RM compounds.
149 The thermal desorption profiles for different RM compounds (Section S4) were compared to pure
150 GOM compounds for which profiles have been developed, including HgO , HgBr_2 , HgCl_2 , HgN_2O_6 ,

151 HgSO₄, and elemental Hg, as well as methylmercury chloride directly added to membranes^{20,21,36}.
152 Thermal desorption profiles have been used to identify Hg compounds not only in ambient air but in
153 other matrices. Exemplarily, Biester and Scholz⁵⁵ developed profiles for solids that have peaks at
154 similar locations as ours for similar compounds.

155 Individual RM compounds were identified from peak deconvolution of thermal desorption
156 profiles^{19,20,24,32}. Each profile was considered to follow a Gaussian distribution (Section S3) and was
157 deconvoluted based on the curve fitting function in MATLAB v. 2018a. Peak temperature ranges were
158 defined for different compounds using an improved calibration system: 80–85 °C for [-O], 90–110 °C
159 for [-Br/Cl], 125–135 °C for [-N], 150–155 °C for [-S], and 180–190 °C for methylmercury (MeHg) or
160 generally organic Hg compounds^{24,32}. To quantify the RM compounds on each nylon membrane, the
161 integral of the area beneath each Gaussian peak was calculated (pg·m⁻³·°C). The relative contribution
162 of each RM compound was calculated based on the integrated peak area. The percentage of the
163 compounds was determined by dividing the concentration of the identified compound using thermal
164 desorption data, specifically the area under the curve, by the total amount of RM measured. RM
165 compound contribution collected on each nylon membrane was determined weekly based on the peak
166 deconvolution analysis. For details on the thermal desorption and peak deconvolution procedures, see
167 Luippold et al.³².

168 **2.5 Back trajectory modeling**

169 The Hybrid Single-Particle Lagrangian Integrated Trajectory model (HYSPLIT, v. 4.2.0), developed
170 by NOAA⁵⁶, was driven with 3-hourly meteorological input data from the Global Data Analysis
171 System (GDAS; 1° latitude-longitude 360 by 181 grid) to identify the potential source regions of RM
172 compounds. The model was run in backward mode for 10 days every 2 hours throughout the CEM and
173 nylon membrane sampling periods at Zeppelin (474 m a.s.l.). In total, ~84 backward trajectories were
174 calculated for each sampling period. The spatial (horizontal and vertical) residence time of the air
175 masses were calculated. The back trajectory model results were combined with five major surface
176 categories – land (no snow cover), open water, permanent ice/snow, sea ice, and snow on land,
177 determined using ESRI ArcGIS Pro (v. 10.6) – to provide the time series of percent surface exposure
178 of particles along trajectories. Moreover, the percent of particles along trajectories that reside within
179 the boundary layer (BL) and in the free troposphere (FT) was analyzed. Details on generation of
180 surface maps and back trajectory statistics are given in section S5.

181 **2.6 GOM/RM dry deposition**

182 **2.6.1 Dry deposition measurements**

183 Three passive Aerohead samplers were deployed to measure GOM dry deposition^{33,34} next to the inlets
184 for the automated and manual RM samplers. GOM was collected on CEM (127 mm diameter, 0.8 µm
185 pore size; Mustang-S, Pall Corporation) on a weekly basis. After each deployment, the three CEM and
186 two non-deployed blanks were collected. The samples were stored in 50 mL centrifuge tubes in

187 double-zipper bags at -20 °C. In the laboratory, the membranes were digested and analyzed identically
188 to the CEM and nylon from the RMAS. Dry deposition of RM was calculated following Lyman et al.
189 ³⁴:

$$190 \quad D = \frac{S-B}{A \cdot T}, \quad (1)$$

191 where D is the deposition rate in ng m⁻² h⁻¹, S is the mass of Hg on the membrane (ng), B is the mass
192 of Hg on the method blanks (ng), A is the surface area of the membrane (0.0104 m²), and T is the
193 deployment duration (h). The mean of all Aerohead CEM blanks was 166 ± 112 pg (1σ, n = 35). The
194 RM dry deposition MDL for a weekly deployment was 0.29 ng m⁻² h⁻¹ (blank + 3σ). Uncertainty in the
195 GOM dry deposition measurements originates from the fact that we measure deposition on an
196 artificial surface and not on snow, ice or tundra vegetation directly, where GOM can be reduced and
197 subsequently re-emitted to the atmosphere. The surface of the CEM provides physical means for
198 understanding temporal changes of GOM dry deposition³⁴.

199 **2.6.2 Dry deposition modeling**

200 Weekly dry deposition of RM was estimated in a three step procedure. First, we determined the
201 individual RM compounds (Hg(OH)₂, HgBr₂/HgCl₂, HgN₂O₆, HgSO₄, MeHg) using thermal
202 desorption and peak deconvolution procedures (Section 2.4). Second, we calculated the RM
203 compound specific dry deposition velocity using a multi-resistance model³⁷. The basic source code of
204 the multi-resistance model was described in Lyman et al.³³ and was subsequently applied by Huang et
205 al.³⁶. Here the code was modified according to the description in section S6, and is publicly accessible
206 (https://github.com/JiaoyanHuang/Dry_Depo_multi_res_model). The meteorological model input
207 parameters were derived from hourly ERA5 data, the fifth generation ECMWF atmospheric reanalysis
208 of the global climate⁵⁷. The meteorological data were representative for a 31 km grid covering the area
209 around Zeppelin. Snow depth was determined at two measurement stations representing a lower and
210 upper limit of snow depth in the area. The first station, representing low snow depth, was located on a
211 measurement field just south of the Ny-Ålesund village; the second station, Bayelva, was located
212 about 3 km outside the village and represented the upper limit of snow depth⁵⁸. Third, we multiplied
213 the RM compound specific dry deposition velocities (calculated by the model) with the relative
214 percentage of the RM compound concentrations measured by the Tekran® or from CEM analysis.

215 **2.7 Uncertainty in RM dry deposition modeling**

216 The uncertainty of the modeled RM dry deposition was assessed using the Monte Carlo simulation
217 approach (Crystal Ball®) and is reported as the 95% confidence interval of 10,000 simulations. The
218 probability distributions of the key input parameters for the model was obtained using the “BatchFit”
219 function in Crystal Ball® based on the dataset for each sampling period. Normal distribution and log-
220 normal distribution were chosen for distribution fitting, and the *p* values for the significance levels of
221 the fitted distributions were all < 0.05. The uncertainty analysis, however, does not include the issues
222 of 1) lower sorption efficiency (ca. 50%) of RM on nylon membranes compared to CEMs and 2) that

223 during peak deconvolution mixed compounds, e.g. HgBrNO_3 , are not well-defined. In order to
224 minimize these uncertainties, the nylon membranes were not used as a quantitative sorption surface
225 but for RM compound analysis only. Several studies have confirmed, that nylon membranes sorbed
226 Hg-Br and Hg-Cl compounds linearly with increasing concentrations (under ambient and laboratory
227 conditions)^{22,53}, and these compounds were neither lost nor transformed RM during sampling and
228 storage⁵³. However, CEM collected systematically higher concentrations of HgBr_2 , HgCl_2 , and a HgO
229 compound²¹. More recent work has demonstrated that the nylon membranes do not effectively collect
230 Hg-N compounds²⁰. We are learning incrementally about the use of membrane for identifying the
231 chemistry of the compounds. Thermal desorption and peak deconvolution procedure introduces
232 uncertainty, because there are only a limited number of RM compounds for which calibration profiles
233 can be developed and currently the desorption profiles are broad. However, comparing the chemistry
234 of the compounds to oxidants measured or expected in the air for a variety of locations, as well as ion
235 chromatography measurement of ions on the nylon membranes, supports the RM chemistry observed.
236 For example, in Hawaii halogenated compounds were dominant, while in Nevada adjacent to a high
237 way N-S-O Hg compounds were present, and in a forested area in Maryland organic compounds were
238 measured²⁴. This indicates that we are effectively getting at the compounds in general, although we do
239 not know the exact chemistry. More work needs to be done to quantify the chemistry and develop
240 surfaces that are better at retaining compounds.

241 **2.8 Auxiliary variables**

242 Meteorological parameters from Zeppelin, including air temperature, wind speed, wind direction,
243 relative humidity, and atmospheric pressure, were provided with an hourly resolution by NILU.
244 Hourly means of tropospheric O_3 concentrations were measured by NILU using a UV absorption
245 spectrometer (API 400A). Hourly means of particulate matter concentrations ($\text{PM}_{2.5}$, PM_{10} , and
246 PM_{total}) were derived from a FIDAS® 200S instrument (Palas GmbH, Germany) operated by
247 Stockholm University (SU). Daily means of particulate and gaseous nitrogen compounds ($\text{HNO}_3/\text{NO}_3^-$,
248 $\text{NH}_4^+/\text{NH}_3$) were collected on a three stage filter pack and analyzed using a Thermo Scientific Dionex
249 Integriion HPIC System equipped with a Dionex AS9-column⁵⁹ and made available by NILU.

250 **3. Results and Discussion**

251 **3.1 Quantification of atmospheric Hg using the Tekran® system**

252 The mean GEM $\pm 1\sigma$ concentration measured between March 26 and July 27, 2019 was 1.36 ± 0.4 ng
253 m^{-3} (Figure 1a). During that period, nine distinct AMDEs were identified, with eight observed in April
254 and May and one in early June. The occurrence of an AMDE was defined when GEM decreased below
255 1 ng m^{-3} ⁴¹ and the O_3 concentration dropped below the 5th percentile ($33 \mu\text{g m}^{-3}$). An AMDE starts
256 when the concentration of GEM sharply decreases and ends when GEM increases again to average
257 concentrations. Due to AMDEs, GEM concentrations in the Arctic are typically the lowest in April

258 and May. From 2000 – 2009³⁹ and 2011 – 2015⁴⁸, 86% and 75%, respectively, of annual observed
 259 AMDEs occurred during the April and May time period. Due to the influence of AMDEs during the
 260 sampling campaign, the mean GEM concentration during the campaign (1.36 ng m^{-3}) was lower than
 261 the annual mean of $1.54 \pm 0.3 \text{ ng m}^{-3}$ measured between 2000 and 2009³⁹ and annual means ranging
 262 from $1.47 - 1.51 \text{ ng m}^{-3}$ between 2011 and 2015⁴⁸. In summer, GEM increases due to re-emission of
 263 previously deposited Hg to surfaces and re-emission of surface Arctic Ocean dissolved Hg^0 ⁶⁰⁻⁶².

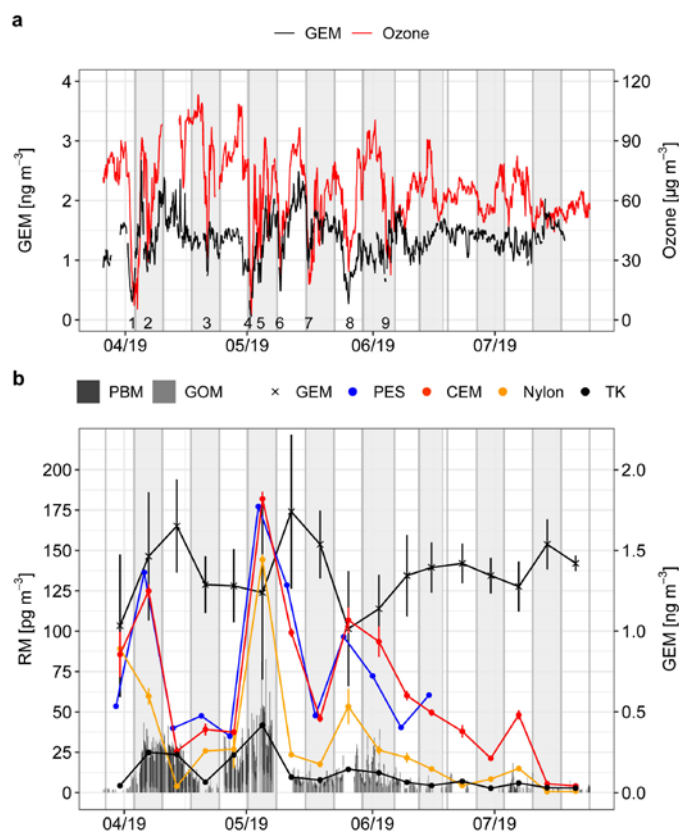


Figure 1: Time series of atmospheric Hg species and O₃ from March 26 to July 27, 2019. (a) GEM (black line) and O₃ (red line) concentrations are displayed as hourly means. AMDEs are indicated with numbers 1 to 9. (b) Mean concentration of GEM (black cross), RM on PES (blue dots), RM on CEM (red dots), and RM on nylon membranes (orange dots). RM from Tekran® (TK) measurements (black dots), as PBM and GOM measurements (gray bars), are also displayed. Error bars represent 1σ and are indicated where $n \geq 3$. PES, CEM, and nylon membranes were deployed for one week. Sampling periods for CEM and nylon membranes are indicated with alternate white and gray backgrounds. The weekly PES sampling was offset from CEM and nylon membrane by one day.

264 Automated Tekran® measurements of RM (GOM+PBM) for the whole sampling campaign were in
 265 the range of $2.6 - 13.1 \text{ pg m}^{-3}$ for GOM and $2.1 - 29.9 \text{ pg m}^{-3}$ for PBM (10th and 90th percentiles). The
 266 mean Tekran® RM concentration (RM_{TK}) was $14.6 \pm 12.7 \text{ pg m}^{-3}$, and the values spanned from below
 267 the MDL to 82.6 pg m^{-3} (Figure 1b). During AMDEs, GOM and PBM concentrations were 9.6 and
 268 20.5 pg m^{-3} , on average, and elevated by 42% and 54%, respectively, compared to the entire campaign
 269 average. These values were at the lower end compared to those measured at Zeppelin during AMDEs
 270 in 2003⁴¹ and in 2007-2008⁴⁷. Overall, RM_{TK} was $< 43.5 \text{ pg m}^{-3}$ (90th percentile) during AMDEs and
 271 lower ($< 30.8 \text{ pg m}^{-3}$, 90th percentile) during the entire campaign.

272 3.2 Quantification of RM using manual methods

273 Mean RM concentration sampled on CEM (RM_{CEM}) was $63 \pm 45 \text{ pg m}^{-3}$ (Section S3). The highest
274 concentrations were found between May 1 and May 8 (182 pg m^{-3}) and lowest at the end of the
275 campaign from July 17 to July 24 (4 pg m^{-3}). The large variation among samples was due to the
276 occurrence of AMDEs until the beginning of June (Figure 1b). Thereafter, RM_{CEM} tended to decrease,
277 with one exception from July 3 to July 10 when RM_{CEM} was 48 pg m^{-3} . The RM concentration on PES
278 (RM_{PES}) was sampled until June 18, 2019 and was similar to RM_{CEM} even though the PES were
279 replaced one day in advance compared to CEM (slope = 0.91, $r^2 = 0.86$; Figure S1a). The mean RM_{PES}
280 was $78 \pm 46 \text{ pg m}^{-3}$, similar to mean RM_{CEM} concentrations for the same period to within 2% (March
281 26 – June 18). The good agreement between the CEM and PES materials was previously demonstrated
282 by Dunham-Cheatham et al.⁵³, showing no significant difference between the two materials ($\alpha = 0.05$).
283 In concert with that study, the nylon membranes in this study were less efficient at capturing RM.
284 The mean RM concentration on nylon membranes (RM_{Nylon}) was $32 \pm 37 \text{ pg m}^{-3}$. The nylon membrane
285 recovery was 50% (range from 12 to 104%) of the RM sorbed on CEM (Figure 1b). The lower RM
286 content on nylon membranes was likely due to the different sorption efficiency of varying RM
287 compounds to this material^{19,20,24,36}. Despite the difference in captured RM, the relationship between
288 RM_{CEM} and RM_{Nylon} was fairly constant ($r^2 = 0.75$, $p < 0.05$, section S3). This supports the conclusions
289 from previous studies that nylon membranes are not suitable for quantitative RM concentrations, but
290 are suitable for thermal desorption analysis to identify RM compounds^{19,53}.
291 Weekly mean RM_{CEM} and RM_{PES} were up to 19 times and 22 times higher compared to RM_{TK} ,
292 respectively (Figure S1b). On average, the RM_{CEM} was 5.3 times and RM_{PES} 5.2 times higher than
293 RM_{TK} based on weekly averages ($11.8 \pm 10.4 \text{ pg m}^{-3}$). Tekran® RM measurements were calculated as
294 the sum of GOM and PBM concentrations and the amount of Hg released during the three 5-min flush
295 cycles (flush_{TK1-3}). The discrepancy between RM on membranes and RM_{TK} agrees with recently
296 performed comparisons, where RM on membranes was 2 to 13 times greater^{17,18,20-22}. However, we
297 would like to point out that the impactor on the Tekran® removes particles with aerodynamic
298 diameters larger than $2.5 \mu\text{m}$ while the membrane-based systems might also capture particles > 2.5
299 μm . The mean $PM_{2.5}$ concentration ($0.97 \mu\text{g m}^{-3}$) was only 30% of the total mean PM concentration
300 ($3.29 \mu\text{g m}^{-3}$) measured during our campaign. Thus, RM_{TK} tend to be lower compared to membrane-
301 based systems due to the lower efficiency of GOM collection⁶³ and due to the exclusion of large PBM
302 ($> 2.5 \mu\text{m}$) from analysis. More multi-season RM_{CEM} and RM_{PES} timeseries at multiple Arctic sites are
303 necessary to derive robust correlations with automated measurements and to potentially correct
304 previous Tekran® RM data.

305 3.3 Compounds of RM

306 Thermal desorption and peak deconvolution revealed the composition of RM species that were
307 retained on the nylon membranes (section S4). The weekly mean RM_{Nylon} ranged from 1 to 144 pg m^{-3}

308 (Figure 2a). The dominant RM compounds sampled over the course of the campaign were Hg-Br/Cl
 309 and Hg-N, that accounted for 51% and 45%, respectively, of the total RM on nylon membranes
 310 (Figure 2b). Organic-based Hg compounds (e.g. MeHg) contributed 2% to the overall RM
 311 concentration. Sulfur compounds (Hg-S) accounted also for 2% while the contribution of oxide
 312 compounds (HgO) was < 1%. The relative contribution of the RM compounds was calculated each
 313 week throughout the campaign (Figure 2c). The Hg-Br/Cl compounds indicate reactions of GEM with
 314 halogens (Cl, Cl₂, Br, Br₂) within the atmospheric BL⁷, where Br• is regarded as one of the primary
 315 first-step atmospheric oxidants to produce RM intermediates such as Hg^IBr^{11,64}. The occurrence of
 316 Hg-N compounds depends on several different factors, such as N emission sources or atmospheric
 317 redox processes occurring between the source and receptor site⁶⁵⁻⁶⁷. Atmospheric NO₂ radicals are also
 318 considered to be the dominant second-step oxidant transforming Hg^IBr to Hg^{II}BrONO in the free
 319 troposphere^{64,68}. During the first sampling deployment week, RM was composed of 34% Hg-Br/Cl
 320 and 58% Hg-N compounds, but in contrast, during week two, 68% Hg-Br/Cl and 32% Hg-N were
 321 detected. During week 6, when two AMDEs occurred and the largest RM concentrations were
 322 measured (182 pg m⁻³), Hg-Br/Cl and Hg-N contributed similar parts to total RM (58% and 42%,
 323 respectively). During weeks seven and eight, the dominant RM compound on the nylon membranes
 324 changed from Hg-N (70%) to Hg-Br/Cl (89%). To explain differences in chemical composition, we
 325 investigated the role of air mass exposure on the dominant RM compounds, Hg-Br/Cl (51%) and Hg-
 326 N (45%), along the air mass back trajectory.

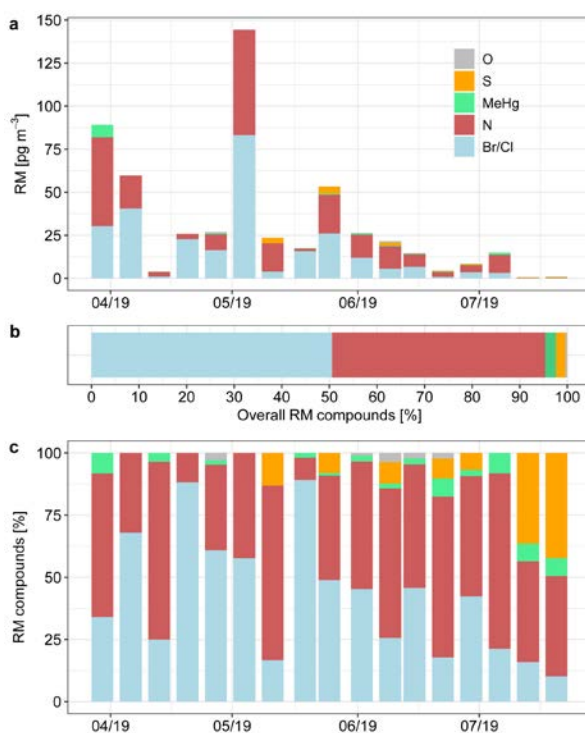


Figure 2: RM compounds determined from March 27 until July 24, 2019. (a) The RM concentration on the nylon membrane from the RMAS for a mixture of RM compounds identified by thermal desorption and peak deconvolution. The frequency distribution of RM compounds, in %, is given (b) for the entire campaign (mean) and (c) for each sampling event.

327 3.4 Origin of RM

328 To investigate if atmospheric conditions influence the RM compounds, the relationship between the
329 trajectories within the BL and in the FT was analyzed. The percentage of time the trajectories arriving
330 at Zeppelin resided in the BL ranged from 7% to 50% (Figure 3a). There was a significant correlation
331 between the percentage of time the trajectories were within the BL and the determined percentage of
332 Hg–Br/Cl compounds ($r^2 = 0.4$, $p < 0.05$). The relationship became even stronger during periods when
333 AMDEs occurred ($r^2 = 0.7$, $p < 0.05$) (Figure 3b). During the same period, Hg–N compounds occurred
334 more frequently when the advected air mass originated from the FT ($r^2 = 0.7$, $p < 0.05$) (Figure 3c).
335 This indicates that air masses enriched in Hg–Br/Cl were in contact with the surface for longer periods
336 compared to air masses enriched in Hg–N, that were originating predominantly in the FT.

337 Air masses arriving at Zeppelin were mainly exposed to sea ice and open water (Figure 3d). The RM
338 concentrations increased when air masses were exposed to sea ice ($r^2 = 0.32$, $p < 0.05$) or land covered
339 by snow ($r^2 = 0.36$, $p < 0.05$) (Figure 3e). Lower RM concentrations were measured when air masses
340 were exposed to open water ($r^2 = 0.43$, $p < 0.05$) (Figure 3f). The positive relationship between Hg–
341 BrCl and the time the air mass passed over sea ice ($p = 0.06$, Figure S4) further corroborates that sea
342 ice and snow on sea ice are the main source of reactive halogen species in the Arctic that oxidize
343 GEM. This can occur via one of two mechanisms, activation from snow on sea ice (surface snow
344 source)⁶⁹ or lofted salty snow particles that form sea salt aerosols within the BL (blowing snow
345 particle source)^{70,71}. Though Hg–Br and Hg–Cl compounds are indistinguishable with our methods, all
346 reactive halogen species in the atmosphere are produced from similar sources, i.e., snow on sea ice and
347 BL aerosols⁷²⁻⁷⁴. In the atmosphere, both Br• and Cl• react with O₃ to form halogen oxides^{75,76}; both
348 halogen radicals and halogen oxides lead to the oxidation of GEM to RM¹⁰.

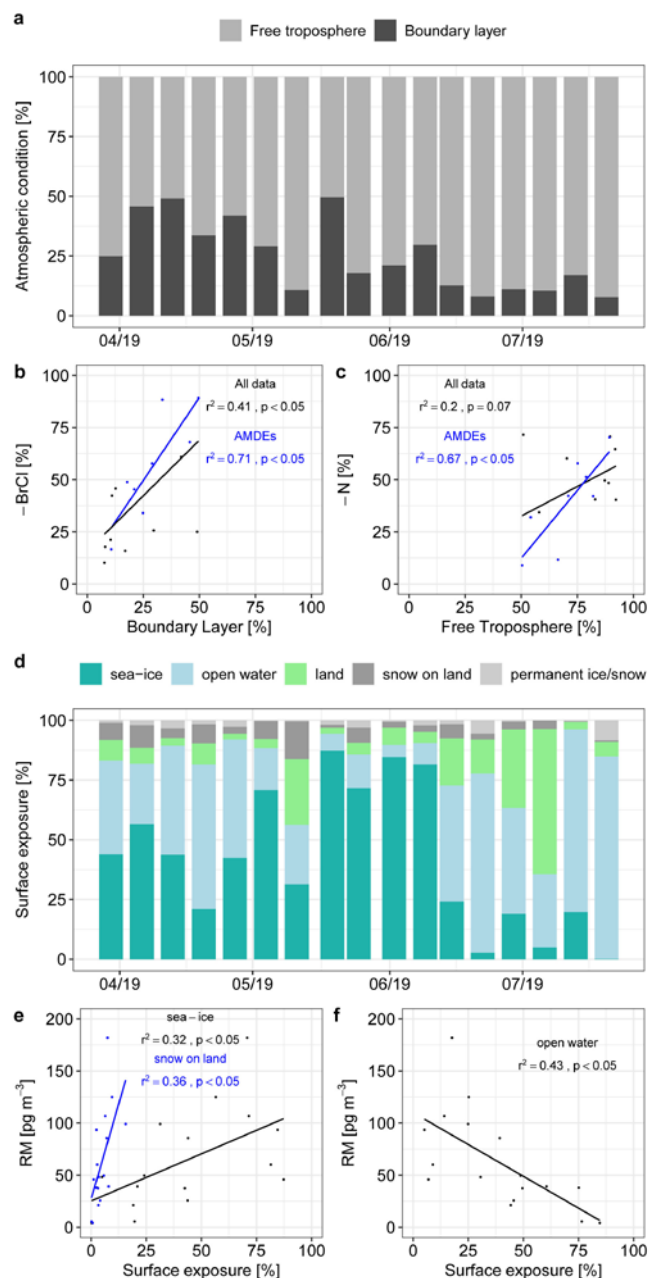


Figure 3: HYSPLIT simulation of air mass trajectory residence time in the atmosphere and exposure to surfaces. (a) Percentage of time the trajectories were in the boundary layer (BL) and free troposphere (FT) for each of the 17 deployment periods. Linear correlation during the entire campaign and during weeks when AMDEs occurred (b) between Hg-Br/Cl and residence time in the BL and (c) Hg-N and residence time in the FT. (d) Surface exposure of trajectories to the 5 major surface categories: sea ice, open water, land (no snow), snow covered land, and permanent ice and snow. Linear correlation between (e) RM_{CEM} and exposure to sea ice and snow covered land, and between (f) RM_{CEM} and exposure to open water.

349 A weak positive relationship between Hg-N and the time the air mass passed over land without snow
 350 cover ($r^2 = 0.2$, $p = 0.06$, Figure S4) indicated an anthropogenic source of N compounds (i.e. NO_2)
 351 from more densely populated areas further south, or more specifically, springtime transport of plumes
 352 from Asian industries or Siberian wildfires⁷⁷. Emitted NO_2 leads to enhanced GEM oxidation and
 353 increased Hg-N concentrations downwind. Though more data are required (multi-seasonal sampling)
 354 to establish significant relationships between RM compounds and exposure time of air masses to

355 different surface types, our conclusions are well illustrated by comparing surface exposure during
356 weeks seven and eight. A maximum of Hg–N compounds was measured during week 7 (70% of total
357 RM), when exposure time of air masses over land (43%) and the residence time in the FT (89%) were
358 long. Back trajectory analysis indicated that the air moved mainly from Fennoscandia (17%) and
359 Siberia (74%) over the eastern Arctic Ocean to Zeppelin (Figure S5g). The Siberian air mass
360 originated from areas where wildfires were ubiquitous between May 8 and May 15, 2019
361 (<https://earthdata.nasa.gov/earth-observation-data/near-real-time/firms>). The mean BL height
362 measured along the air mass trajectories was 277 m a.s.l and was elevated compared to week 8 (87 m
363 a.s.l). In week 8, Hg–Br/Cl was the dominant RM compound (89%) and air masses passed
364 predominantly over sea ice (87%) from areas east of Zemlya Georga and northwest of Svalbard to
365 Zeppelin (Figure S5h). The residence time of the air mass in the BL was 50%, which corresponded to
366 the longest residence time in the BL among all weeks of sampling (Figure 3a). Thus, the
367 comparatively long residence time of air masses within the BL over the sea ice-covered Arctic Ocean
368 constituted the main source region of Hg–Br/Cl arriving at Zeppelin.

369 **3.5 Dry deposition measurements and modeling**

370 Mean local GOM dry deposition at Zeppelin measured by Aerohead samplers was $0.35 \text{ ng m}^{-2} \text{ h}^{-1}$, and
371 weekly averages ranged from below the MDL to $1.47 \text{ ng m}^{-2} \text{ h}^{-1}$ (Figure 4). Measurements of GOM
372 dry deposition in 9 out of 17 weeks were above the MDL ($0.29 \text{ ng m}^{-2} \text{ h}^{-1}$). The cumulative Aerohead
373 GOM dry deposition measured from March 27 to July 24, 2019 was $1 \text{ } \mu\text{g m}^{-2}$, with a 95% confidence
374 interval ranging from 0.74 to $1.25 \text{ } \mu\text{g m}^{-2}$ (Figure 4). Dry deposition of GOM measured by Aerohead
375 samplers was negligible ($< 0.1\%$ of the cumulative flux) during the last 5 weeks of measurements
376 (June 19 to July 27, 2019). During weeks 3 and 4, there was less than 1 pg GOM measured on the
377 Aerohead CEM, in contrast to 795 pg analyzed on the CEMs from RMAS indicating the importance of
378 particulate-bound Hg. During weeks 5 and 9, measured GOM dry deposition exceeded the modeled
379 RM dry deposition by 38% and 43%, respectively. A comparison of meteorological and chemical
380 variables during these weeks with the preceding and following weeks indicated no unusual conditions.
381 It could be a compound was present that was sticking to the open-faced membranes in the Aeroheads,
382 but not making its way into the filter packs holding membranes in the RMAS or the compound had a
383 higher deposition velocity than other compounds. This would be true for HgO that once formed is
384 thought to become a particle and rapidly deposit to surfaces⁷⁸. Thus, understanding reactions forming
385 and the chemistry of compounds of GOM/RM is greatly needed.

386 The cumulative modeled dry deposition of RM, based on RM compound-specific dry deposition
387 velocities and RM_{TK} , was $0.33 \text{ } \mu\text{g m}^{-2}$ with a 95% confidence interval ranging from 0.23 to $0.50 \text{ } \mu\text{g m}^{-2}$
388 (Figure 4). The modeled flux was one-third of the measured flux. The average RM dry deposition
389 velocities of $\text{Hg}(\text{OH})_2$, $\text{HgBr}_2/\text{HgCl}_2$, HgN_2O_6 , HgSO_4 , MeHg were very similar and differed by less
390 than 5% during each sampling week (Table S6). The dominant RM compounds $\text{HgBr}_2/\text{HgCl}_2$ and

391 HgN_2O_6 both exhibited a mean deposition velocity of $0.28 \pm 0.10 \text{ cm s}^{-1}$ over the course of the
 392 campaign. The weekly mean RM deposition velocities ranged from 0.12 cm s^{-1} (week 15) to 0.48 cm s^{-1}
 393 $^{-1}$ (week 10). The mean deposition velocity of all RM compounds was $0.32 \pm 0.09 \text{ cm s}^{-1}$ when the area
 394 around Zeppelin was covered by snow, and $0.21 \pm 0.08 \text{ cm s}^{-1}$ during the last five weeks of
 395 measurements when snowmelt had occurred (June 17, 2019).

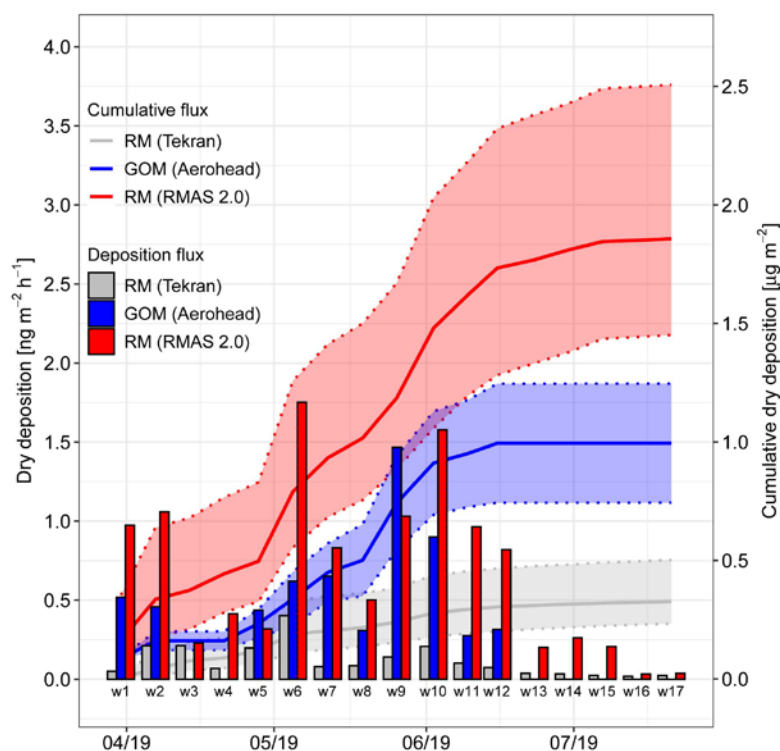


Figure 4: Measured GOM and modeled RM dry deposition for the entire sampling period. Weekly GOM dry deposition calculated based on the Aerohead system (measured) and RM dry deposition estimated based on the Tekran® and RMAS systems using RM compound-specific dry deposition velocities (modeled). The cumulative flux over the entire sampling campaign (lines) and associated uncertainties (shaded area, 95% confidence interval) are given.

396 The modeled cumulative dry deposition based on RM_{CEM} was $1.86 \mu\text{g m}^{-2}$ with a 95% confidence
 397 interval ranging from 1.45 to $2.50 \mu\text{g m}^{-2}$ (Figure 4). Thus, RM dry deposition was 5.6 times larger
 398 compared to estimates using Tekran® data (Table S7). The discrepancy between the measured
 399 (Aerohead) and the modeled (RMAS) cumulative dry deposition, a factor of 1.9, was due to the
 400 Aerohead sampling GOM, while PBM adsorbs negligibly to the down-facing surrogate surface due to
 401 gravity^{22,34-36,79-81}. The inconsistency during weeks 1, 2, and 6 could accordingly be explained by
 402 elevated concentrations of particulate matter (PM_{total}), indicating that PBM dominated RM dry
 403 deposition during these weeks (Figure S2). The inconsistency in weeks 10, 11 and 12, however, was
 404 likely associated with elevated RM dry deposition velocities (0.47 cm s^{-1}), given the low PBM
 405 concentrations, as compared to the other weeks (0.25 cm s^{-1}) that are not reproduced by the Aerohead
 406 measurements. It is likely that Hg–N RM compounds were advected on particles, especially during
 407 weeks 1 and 6 when the absolute amount of Hg–N RM compounds was elevated (Figure 2a). During
 408 the entire campaign, though, the ammonium (NH_4^+) and nitrate (NO_3^-) aerosol concentration was at
 409 least three orders of magnitude higher compared to the concentrations of Hg–N compounds. This

410 indicates that RM production and transformation of Hg–N compounds was not directly linked to
411 advection of particulate nitrogen compounds, which is consistent with a predominant gas-phase
412 oxidation of RM precursor by NO₂ in the FT⁶⁴.

413 **3.6 Implications**

414 Arctic RM concentrations analyzed on CEM and PES were higher than Tekran® RM during all weeks
415 of measurements. That the Tekran® system significantly underestimated RM concentrations in the
416 Arctic was surprising since one would expect that most of the RM would be Br and Cl compounds and
417 given the efficiency of the denuder the KCl denuder it should be 1.2 to 1.3 times lower as
418 demonstrated in Huang et al.,²¹. But Huang et al.²¹'s experiments were done in clean air whereas the
419 measurements in the Arctic were of ambient air, indicating the impact of some aspect atmospheric
420 chemistry (e.g. O₃) on retention of GOM compounds. The difference between RM concentrations was
421 large during the AMDE season (mainly April and May) and became small when the RM
422 concentrations decreased in the summer. In general, RM_{TK} showed a significant, but not strong,
423 correlation ($r^2 < 0.6$) with RM_{CEM} and RM_{PES}. Bias in denuder-based Tekran® quantification of GOM
424 could not be corrected, as was suggested for the Pic du Midi high-altitude site in the Pyrenees,
425 France²⁵. The bias in Arctic RM concentration measurements between manual and automated methods
426 must be addressed not only during AMDEs but with multi-seasonal sampling campaigns at sites such
427 as Alert in Canada, where Tekran® systems are also operated year-round.

428 RM compound-specific deposition velocity estimates provide the way for more accurate RM dry
429 deposition estimates. However, as stated in Gustin et al.⁶³, the determination of RM compounds could
430 be improved by: 1) using a new thermal desorption surface, because the nylon membranes
431 underestimate RM concentrations (by 50% in this study); and 2) identifying the exact chemistry of
432 RM compounds by developing a mass spectrometry method.

433 The RM dry deposition model revealed higher fluxes when using the RMAS data compared to
434 Tekran® data, suggesting a 5.6 times larger input of RM to Arctic ecosystems. In the Ny-Ålesund
435 area, RM dry deposition (1.9 µg m⁻² from March 27 to July 24, 2019) was the dominant Hg deposition
436 pathway, exceeding mean annual wet deposition ranging from 0.8 to 1.7 µg m⁻² yr⁻¹ measured between
437 2012 and 2015⁸².

438 If we accept the assumption that dry deposition measurements made by the Aerohead system are
439 accurate for GOM and measurements performed with RMAS are accurate for RM, our results
440 demonstrate that RM bound to particles constituted 46% of the deposited Hg; this also assumes that
441 RM dry deposition occurs homogeneously and independently of different boundary layer conditions at
442 Zeppelin. In fact, large particles > PM_{2.5} (not analyzed by the Tekran®) contributed 70% to the total
443 PM concentration (Figure S2). This indicates that a dominant portion of the RM was associated with
444 large particles (> PM_{2.5}), likely marine aerosols. Our study showed that RM dry deposition estimates

445 during the 2019 AMDE season at Zeppelin, and potentially elsewhere in the Arctic, were likely higher
446 than previously assumed and reported. This has implications for the amount of Hg cycling between the
447 atmosphere and Arctic ecosystems.

448 **Associated content (Supporting Information)**

449 The Supporting Information (SI) is available free of charge on the ACS publication website. The SI is
450 structured in six different sections (S1 – S6). We provide details on automated (S1) and manual (S2)
451 RM sampling and analysis as well as an overview of the measured RM concentrations (S3). The
452 thermal desorption procedure is described and profiles displayed (S4). Back trajectory modeling is
453 detailed in S5 and supplementary information about dry deposition modeling is given in S6.

454 **Author information (corresponding author)**

455 Stefan Osterwalder - Institute of Agricultural Sciences, ETH Zurich, Universitätsstrasse 2, 8092
456 Zurich, Switzerland; orcid.org/0000-0001-8775-0813; Phone: +41 76 477 35 89; Email:
457 stefan.osterwalder@usys.ethz.ch

458 **Financial sources**

459 This research was funded by the French Polar Institute IPEV (Programme 1207 MESSI), the EC
460 H2020 ERA-PLANET (grant no. 689443) iGOSP and iCUPE programmes. The project also received
461 funding from the Swiss National Science Foundation (SNSF) project P400P2_180796 and the NSF
462 project 1700711.

463 **Acknowledgements**

464 We thank the following persons for assistance in the field and laboratory: Laure Laffont from GET,
465 Ove Hermansen and Are Bäcklund from NILU, Christelle Guesnon from NPI and all personnel from
466 IPEV and Alfred Wegener Institute (AWI) for Polar and Marine Research. We acknowledge Hans-
467 Werner Jacobi from Université Grenoble Alpes, Julia Boike, Christian Lehr and Siegrid Debatin from
468 AWI for providing snow depth data. We are grateful to Paul Zieger from SU for providing PM data
469 from Zeppelin. We would like to thank Wenche Aas (NILU) for making data on particulate and
470 gaseous nitrogen compounds available. The student assistants from the University of Nevada, Reno
471 lab are acknowledged for their support with membrane digestion and analysis. The authors thank 3
472 anonymous reviewers for their comments.

473 **Data availability**

474 RM concentration data are given in the Supporting Information. A detailed model description is
475 provided in https://github.com/JiaoyanHuang/Dry_Depo_multi_res_model. Raw data on thermal
476 desorption and peak deconvolution procedures or from back trajectory modeling are available on
477 request.

478 **References**

- 479 (1) AMAP Assessment 2011: Mercury in the Arctic., Arctic Monitoring and Assessment Programme
480 (AMAP), Oslo, Norway., **2011**.
- 481 (2) Douglas, T.A., Loseto, L.L., Macdonald, R.W., Outridge, P., Dommergue, A., Poulain, A., Amyot,
482 M., Barkay, T., Berg, T., Chételat, J., Constant, P., Evans, M., Ferrari, C., Gantner, N., Johnson,
483 M.S., Kirk, J., Kroer, N., Larose, C., Lean, D., Nielsen, T.G., Poissant, L., Rognerud, S., Skov, H.,
484 Sørensen, S., Wang, F., Wilson, S. Zdanowicz, C.M. The fate of mercury in Arctic terrestrial and
485 aquatic ecosystems, a review. *Environ. Chem.* **2012**, 9, 321-355. <http://dx.doi.org/10.1071/EN11140>
- 486 (3) UNEP Minamata Convention on Mercury: Text and Annexes. UNEP Chemicals Branch, Geneva,
487 Switzerland, **2013**. <http://www.mercuryconvention.org> (last access: 12. April 2021).
- 488 (4) Soerensen, A.L., Jacob, D.J., Schartup, A.T., Fisher, J.A., Lehnerr, I., Louis, V.L.S., Heimbürger,
489 L.-E., Sonke, J.E., Krabbenhoft, D.P., Sunderland, E.M. A mass budget for mercury and
490 methylmercury in the Arctic Ocean. *Glob. Biogeochem. Cycles* **2016**, 30, 560–575.
491 <https://doi.org/10.1002/2015GB005280>
- 492 (5) Dastoor, A.P. and Durnford, D.A. Arctic Ocean: Is It a Sink or a Source of Atmospheric Mercury?
493 *Environ. Sci. Technol.* **2014**, 48, 1707-1717. <https://doi.org/10.1021/es404473e>
- 494 (6) Schroeder, W.H., Anlauf, K.G., Barrie, L.A., Lu, J.Y., Steffen, A., Schneeberger, D.R., Berg, T.
495 Arctic springtime depletion of mercury. *Nature* **1998**, 394, 331–332. <https://doi.org/10.1038/28530>
- 496 (7) Ariya, P.A., Dastoor, A.P., Amyot, M., Schroeder, W.H., Barrie, L., Anlauf, K., Raofie, F.,
497 Ryzhkov, A., Davignon, D., Lalonde, J., Steffen, A. The Arctic: a sink for mercury. *Tellus B:*
498 *Chemical and Physical Meteorology* **2004**, 56, 397–403. <https://doi.org/10.3402/tellusb.v56i5.16458>
- 499 (8) Skov, H., Christensen, J. H., Goodsite, M. E., Heidam, N. Z., Jensen, B., Wählin, P., Geernaert, G.
500 Fate of elemental mercury in the arctic during atmospheric mercury depletion episodes and the load
501 of atmospheric mercury to the arctic. *Environ. Sci. Technol.* **2004**, 38, 2373–2382.
502 <https://doi.org/10.1021/es030080h>
- 503 (9) Lindberg, S. E., Brooks, S., Lin, C.-J., Scott, K. J., Landis, M. S., Stevens, R. K., Goodsite, M. E.,
504 Richter, A. Dynamic oxidation of gaseous mercury in the arctic troposphere at polar sunrise. *Environ.*
505 *Sci. Technol.* **2002**, 36, 1245–1256. <https://doi.org/10.1021/es0111941>
- 506 (10) Steffen, A., T. Douglas, M. Amyot, P. Ariya, K. Aspomo, T. Berg, J. Bottenheim, S. Brooks, F.
507 Cobbett, A. Dastoor, A. Dommergue, R. Ebinghaus, C. Ferrari, K. Gardfeldt, M.E. Goodsite, D.
508 Lean, A.J. Poulain, C. Scherz, H. Skov, J. Sommar, Temme, C. A synthesis of atmospheric mercury
509 depletion event chemistry in the atmosphere and snow. *Atmos. Chem. and Phys.* **2008**, 8, 1445–1482.
510 <https://doi.org/10.5194/acp-8-1445-2008>
- 511 (11) Wang, S., McNamara, S.M., Moore, C.W., Obrist, D., Steffen, A., Shepson, P.B., Staebler, R.M.,
512 Raso, A.R.W., Pratt, K.A. Direct detection of atmospheric atomic bromine leading to mercury and
513 ozone depletion. *PNAS* **2019**, 116, 14479–14484. <https://doi.org/10.1073/pnas.1900613116>
- 514 (12) Obrist, D., Agnan, Y., Jiskra, M., Olson, C.L., Colegrove, D.P., Hueber, J., Moore, C.W., Sonke,

- 515 J.E., Helmig, D. Tundra uptake of atmospheric elemental mercury drives Arctic mercury pollution.
516 *Nature* **2017**, 547, 201–204. <https://www.nature.com/articles/nature22997>
- 517 (13) Dommergue, A., Larose, C., Fain, X., Clarisse, O., Foucher, D., Hintelmann, H., Schneider, D.,
518 Ferrari, C.P. Deposition of Mercury Species in the Ny-Ålesund Area (79°N) and Their Transfer
519 during Snowmelt. *Environ. Sci. Technol.* **2010**, 44, 901–907. <https://doi.org/10.1021/es902579m>
- 520 (14) Steffen, A., Bottenheim, J., Cole, A., Ebinghaus, R., Lawson, G., Leaitch, W. R. Atmospheric
521 mercury speciation and mercury in snow over time at Alert, Canada, *Atmos. Chem. Phys.* **2014**, 14,
522 2219–2231. <https://doi.org/10.5194/acp-14-2219-2014>
- 523 (15) Kamp, J., Skov, H., Jensen, B., Sørensen, L.L. Fluxes of gaseous elemental mercury (GEM) in the
524 High Arctic during atmospheric mercury depletion events (AMDEs). *Atmos. Chem. Phys.* **2018**, 18,
525 6923–6938. <https://doi.org/10.5194/acp-18-6923-2018>
- 526 (16) Jiskra, M., Sonke, J.E., Agnan, Y., Helmig, D., Obrist, D. Insights from mercury stable isotopes on
527 terrestrial–atmosphere exchange of Hg(0) in the Arctic tundra. *Biogeosciences* **2019**, 16, 4051–4064.
528 <https://doi.org/10.5194/bg-16-4051-2019>
- 529 (17) Gustin, M. S.; Huang, J.; Miller, M. B.; Peterson, C.; Jaffe, D. A.; Ambrose, J.; Finley, B. D.;
530 Lyman, S. N.; Call, K.; Talbot, R.; Feddersen, D.; Mao, H.; Lindberg, S. E. Do We Understand What
531 the Mercury Speciation Instruments Are Actually Measuring? Results of RAMIX. *Environ. Sci.*
532 *Technol.* **2013**, 47, 7295–7306.
- 533 (18) Gustin, M.S., Amos, H.M., Huang, J., Miller, M.B., Heidecorn, K. Measuring and modeling mercury
534 in the atmosphere: a critical review. *Atmos. Chem. Phys.* **2015**, 15, 5697–5713.
535 <https://doi.org/10.5194/acp-15-5697-2015>
- 536 (19) Gustin, M.S., Dunham-Cheatham, S.M., Zhang, L. Comparison of 4 Methods for Measurement of
537 Reactive, Gaseous Oxidized, and Particulate Bound Mercury. *Environ. Sci. Technol.* **2019**, 53,
538 14489–14495. <https://doi.org/10.1021/acs.est.9b04648>
- 539 (20) Gustin, M.S., Dunham-Cheatham, S.M., Zhang, L., Lyman, S., Choma, N., Castro, M. Use of
540 Membranes and Detailed HYSPLIT Analyses to Understand Atmospheric Particulate, Gaseous
541 Oxidized, and Reactive Mercury Chemistry. *Environ. Sci. Technol.* **2021a**, 55, 893–901.
542 <https://doi.org/10.1021/acs.est.0c07876>
- 543 (21) Huang, J.; Miller, M. B.; Weiss-Penzias, P.; Gustin, M. S. Comparison of Gaseous Oxidized Hg
544 Measured by KCl-Coated Denuders, and Nylon and Cation Exchange Membranes. *Environ. Sci.*
545 *Technol.* **2013**, 47, 7307–7316. <https://doi.org/10.1021/es4012349>
- 546 (22) Huang, J., Miller, M.B., Edgerton, E., Gustin, M.S. Use of criteria pollutants, active and passive
547 mercury sampling, and receptor modeling to understand the chemical forms of gaseous oxidized
548 mercury in Florida. *Atmos. Chem. Phys. Discuss.* **2015**, 12069–12105. <https://doi.org/10.5194/acpd-15-12069-2015>
- 550 (23) McClure, C.D., Jaffe, D.A., Edgerton, E.S. Evaluation of the KCl Denuder Method for Gaseous
551 Oxidized Mercury using HgBr₂ at an In-Service AMNet Site. *Environ. Sci. Technol.* **2014**, 48,

- 552 11437–11444. <https://doi.org/10.1021/es502545k>
- 553 (24) Luippold, A., Gustin, M.S., Dunham-Cheatham, S.M., Castro, M., Luke, W., Lyman, S., Zhang, L.
554 Use of Multiple Lines of Evidence to Understand Reactive Mercury Concentrations and Chemistry in
555 Hawai'i, Nevada, Maryland, and Utah, USA. *Environ. Sci. Technol.* **2020a**, 54, 7922–7931.
556 <https://doi.org/10.1021/acs.est.0c02283>
- 557 (25) Maruszczak, N., Sonke, J.E., Fu, X., Jiskra, M. Tropospheric GOM at the Pic du Midi Observatory –
558 correcting bias in denuder based observations. *Environ. Sci. Technol.* **2017**, 51, 863–869.
559 <https://doi.org/10.1021/acs.est.6b04999>
- 560 (26) Lynam, M.M., and Keeler, G.J. Artifacts associated with the measurement of particulate mercury in
561 an urban environment: The influence of elevated ozone concentrations. *Atmospheric Environ.* **2005**,
562 39, 3081–3088. <http://dx.doi.org/10.1016/j.atmosenv.2005.01.036>
- 563 (27) Malcolm, E.G., and Keeler, G.J.: Evidence for a sampling artifact for particulate-phase mercury in
564 the marine atmosphere, *Atmospheric Environ.* **2007**, 41, 3352–3359.
565 <https://doi.org/10.1016/j.atmosenv.2006.12.024>
- 566 (28) Rutter, A.P., Hanford, K.L., Zwiers, J.T., Perillo-Nicholas, A.L. Evaluation of an offline method for
567 the analysis of atmospheric reactive gaseous mercury and particulate mercury. *J. Air Waste Manag.*
568 *Assoc.* **2008**, 58, 377–383. <https://doi.org/10.3155/1047-3289.58.3.377>
- 569 (29) Kos, G., Ryzhkov, A., Dastoor, A., Narayan, J., Steffen, A., Ariya, P. A., Zhang, L. Evaluation of
570 discrepancy between measured and modelled oxidized mercury species, *Atmos. Chem. Phys.* **2013**,
571 13, 4839–4863. <https://doi.org/10.5194/acp-13-4839-2013>
- 572 (30) Talbot, R., Mao, H., Feddersen, D., Smith, M., Kim, S.Y., Sive, B., Haase, K., Ambrose, J., Zhou,
573 Y., Russo, R. Comparison of Particulate Mercury Measured with Manual and Automated Methods.
574 *Atmosphere* **2011**, 2, 1–20. <https://doi.org/10.3390/atmos2010001>
- 575 (31) Feddersen, D.M., Talbot, R., Mao, H., Sive, B.C. Size distribution of particulate mercury in marine
576 and coastal atmospheres. *Atmos. Chem. Phys.* **2012**, 12, 10899–10909. <https://doi.org/10.5194/acp-12-10899-2012>
- 577
- 578 (32) Luippold, A., Gustin, M.S., Dunham-Cheatham, S.M., Zhang, L. Improvement of quantification and
579 identification of atmospheric reactive mercury. *Atmospheric Environ.* **2020b**, 224, 117307.
580 <https://doi.org/10.1016/j.atmosenv.2020.117307>
- 581 (33) Lyman, S.N., Gustin, M.S., Prestbo, E.M., Marsik, F.J. Estimation of Dry Deposition of Atmospheric
582 Mercury in Nevada by Direct and Indirect Methods. *Environ. Sci. Technol.* **2007**, 41, 1970–1976.
583 <https://doi.org/10.1021/es062323m>
- 584 (34) Lyman, S.N., Gustin, M.S., Prestbo, E.M., Kilner, P.I., Edgerton, E., Hartsell, B. Testing and
585 Application of Surrogate Surfaces for Understanding Potential Gaseous Oxidized Mercury Dry
586 Deposition. *Environ. Sci. Technol.* **2009**, 43, 6235–6241. <https://doi.org/10.1021/es901192e>
- 587 (35) Gustin, M.S, Weiss-Penzias, P.S., Peterson, C. Investigating sources of gaseous oxidized mercury in
588 dry deposition at three sites across Florida, USA. *Atmos. Chem. Phys.* **2012**, 12, 9201–9219.

- 589 <https://doi.org/10.5194/acp-12-9201-2012>
- 590 (36) Huang, J., Miller, M.B., Edgerton, E., Gustin, M.S. Deciphering potential chemical compounds of
591 gaseous oxidized mercury in Florida, USA. *Atmos. Chem. Phys.* **2017**, 17, 1689–1698.
592 <https://doi.org/10.5194/acp-17-1689-2017>
- 593 (37) Zhang, L., Brook, J.R., Vet, R. A revised parameterization for gaseous dry deposition in air-quality
594 models. *Atmos. Chem. Phys.* **2003**, 3, 2067–2082. <https://doi.org/10.5194/acp-3-2067-2003>
- 595 (38) Berg, T., Bartnicki, J., Munthe, J., Lattila, H., Hrehoruk, J., Mazur, A. Atmospheric mercury species
596 in the European Arctic: Measurements and modelling. *Atmospheric Environ.* **2001**, 35, 2569–2582.
597 [https://doi.org/10.1016/S1352-2310\(00\)00434-9](https://doi.org/10.1016/S1352-2310(00)00434-9)
- 598 (39) Berg, T., Pfaffhuber, K.A., Cole, A.S., Engelsen, O., Steffen, A.. Ten-year trends in atmospheric
599 mercury concentrations, meteorological effects and climate variables at Zeppelin, Ny-Ålesund.
600 *Atmos. Chem. Phys.* **2013**, 13, 6575–6586. <https://doi.org/10.5194/acp-13-6575-2013>
- 601 (40) Berg, T., Sekkesæter, S., Steinnes, E., Valdal, A.-K., Wibetoe, G. Springtime depletion of mercury in
602 the European Arctic as observed at Svalbard. *Sci. Total Environ.* **2003**, Pathways and processes of
603 mercury in the environment. Selected papers presented at the sixth International Conference on
604 Mercury as Global Pollutant, Minamata, Japan, Oct. 15-19, 2001 304, 43–51.
605 [https://doi.org/10.1016/S0048-9697\(02\)00555-7](https://doi.org/10.1016/S0048-9697(02)00555-7)
- 606 (41) Aspmo, K., Gauchard, P.-A., Steffen, A., Temme, C., Berg, T., Bahlmann, E., Banic, C.,
607 Dommergue, A., Ebinghaus, R., Ferrari, C., Pirrone, N., Sprovieri, F., Wibetoe, G. Measurements of
608 atmospheric mercury species during an international study of mercury depletion events at Ny-
609 Ålesund, Svalbard, spring 2003. How reproducible are our present methods? *Atmospheric Environ.*
610 **2005**, 39, 7607–7619. <https://doi.org/10.1016/j.atmosenv.2005.07.065>
- 611 (42) Gauchard, P.-A., Aspmo, K., Temme, C., Steffen, A., Ferrari, C., Berg, T., Ström, J., Kaleschke, L.,
612 Dommergue, A., Bahlmann, E., Magand, O., Planchon, F., Ebinghaus, R., Banic, C., Nagorski, S.,
613 Baussand, P., Boutron, C. Study of the origin of atmospheric mercury depletion events recorded in
614 Ny-Ålesund, Svalbard, spring 2003. *Atmospheric Environ.* **2005**, 39, 7620–7632.
615 <https://doi.org/10.1016/j.atmosenv.2005.08.010>
- 616 (43) Sprovieri, F., Pirrone, N., Landis, M.S., Stevens, R.K. Oxidation of Gaseous Elemental Mercury to
617 Gaseous Divalent Mercury during 2003 Polar Sunrise at Ny-Ålesund. *Environ. Sci. Technol.* **2005a**,
618 39, 9156–9165, <https://doi.org/10.1021/es050965o>
- 619 (44) Sprovieri, F., Pirrone, N., Landis, M.S., Stevens, R.K. Atmospheric mercury behavior at different
620 altitudes at Ny-Ålesund during Spring 2003. *Atmospheric Environ.* **2005b**, 39, 7646–7656.
621 <https://doi.org/10.1016/j.atmosenv.2005.08.001>
- 622 (45) Sommar, J., Wängberg, I., Berg, T., Gårdfeldt, K., Munthe, J., Richter, A., Urba, A., Wittrock, F.,
623 Schroeder, W. H. Circumpolar transport and air-surface exchange of atmospheric mercury at Ny-
624 Ålesund (79° N), Svalbard, spring 2002. *Atmos. Chem. Phys.* **2007**, 7, 151–166, doi:10.5194/acp-7-
625 151-2007

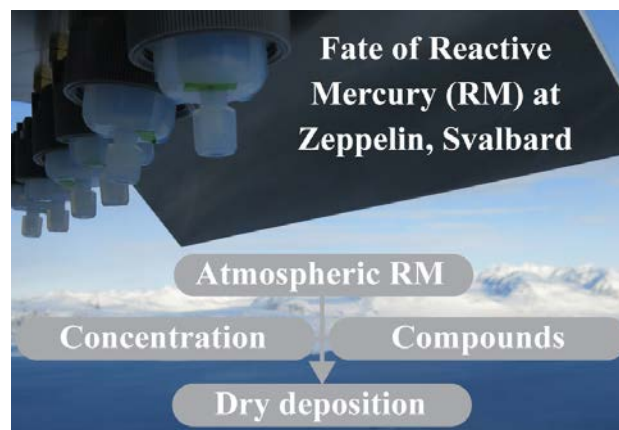
- 626 (46) Ferrari, C.P., Padova, C., Faïn, X., Gauchard, P.-A., Dommergue, A., Aspino, K., Berg, T., Cairns,
627 W., Barbante, C., Cescon, P., Kaleschke, L., Richter, A., Wittrock, F., Boutron, C. Atmospheric
628 mercury depletion event study in Ny-Alesund (Svalbard) in spring 2005. Deposition and
629 transformation of Hg in surface snow during springtime. *Sci. Total Environ.* **2008**, 397, 167–177.
630 <https://doi.org/10.1016/j.scitotenv.2008.01.064>
- 631 (47) Steen, A.O., Berg, T., Dastoor, A.P., Durnford, D.A., Engelsen, O., Hole, L.R., Pfaffhuber, K.A.
632 Natural and anthropogenic atmospheric mercury in the European Arctic: a fractionation study. *Atmos.*
633 *Chem. Phys.* **2011**, 11, 6273–6284. <https://doi.org/10.5194/acp-11-6273-2011>
- 634 (48) Angot, H., Dastoor, A., De Simone, F., Gårdfeldt, K., Gencarelli, C.N., Hedgecock, I.M., Langer, S.,
635 Magand, O., Mastromonaco, M.N., Nordstrøm, C., Pfaffhuber, K.A., Pirrone, N., Ryjkov, A., Selin,
636 N.E., Skov, H., Song, S., Sprovieri, F., Steffen, A., Toyota, K., Travnikov, O., Yang, X.,
637 Dommergue, A. Chemical cycling and deposition of atmospheric mercury in polar regions: review of
638 recent measurements and comparison with models. *Atmos. Chem. Phys.* **2016**, 16, 10735–10763.
639 <https://doi.org/10.5194/acp-16-10735-2016>
- 640 (49) Landis, M.S., Stevens, R.K., Schaedlich, F., Prestbo, E.M. Development and Characterization of an
641 Annular Denuder Methodology for the Measurement of Divalent Inorganic Reactive Gaseous
642 Mercury in Ambient Air. *Environ. Sci. Technol.* **2002**, 36, 3000–3009.
643 <https://doi.org/10.1021/es015887t>
- 644 (50) Steffen, A., Scherz, T., Olson, M., Gay, D., Blanchard, P. A comparison of data quality control
645 protocols for atmospheric mercury speciation measurements. *J. Environ. Monit.* **2012**, 14, 752–765.
646 <https://doi.org/10.1039/C2EM10735J>
- 647 (51) D’Amore, F., Bencardino, M., Cinnirella, S., Sprovieri, F., Pirrone, N. Data quality through a web-
648 based QA/QC system: implementation for atmospheric mercury data from the global mercury
649 observation system. *Environ. Sci.: Processes Impacts* **2015**, 17, 1482–1491.
650 <https://doi.org/10.1039/C5EM00205B>
- 651 (52) Enrico, M., Le Roux, G., Maruszczak, N., Heimbürger, L.-E., Claustres, A., Fu, X., Sun, R., Sonke,
652 J.E. Atmospheric mercury transfer to peat bogs dominated by gaseous elemental mercury dry
653 deposition. *Environ. Sci. Technol.* **2016**, 50, 2405–2412. <https://doi.org/10.1021/acs.est.5b06058>
- 654 (53) Dunham-Cheatham, S.M., Lyman, S., Gustin, M.S. Evaluation of sorption surface materials for
655 reactive mercury compounds. *Atmospheric Environ.* **2020**, 242, 117836.
656 <https://doi.org/10.1016/j.atmosenv.2020.117836>
- 657 (54) Miller, M.B., Dunham-Cheatham, S.M., Gustin, M.S., Edwards, G.C. Evaluation of cation exchange
658 membrane performance under exposure to high Hg⁰ and HgBr₂ concentrations. *Atmos. Meas. Tech.*
659 **2019**, 12, 1207–1217. <https://doi.org/10.5194/amt-12-1207-2019>
- 660 (55) Biester, H. and Scholz, C. Determination of Mercury Binding Forms in Contaminated Soils: Mercury
661 Pyrolysis versus Sequential Extractions. *Environ. Sci. Technol.* **1996**, 31, 233–239.
662 <https://doi.org/10.1021/es960369h>
- 663 (56) Stein, A.F., Draxler, R.R., Rolph, G.D., Stunder, B.J.B., Cohen, M.D., Ngan, F. NOAA’s HYSPLIT

- 664 Atmospheric Transport and Dispersion Modeling System. *Bull. Ame. Meteorol. Soc.* **2015**, 96, 2059–
665 2077. <https://doi.org/10.1175/BAMS-D-14-00110.1>
- 666 (57) Hersbach, H., Bell, B., Berrisford, P., Hirahara, S., Horányi, A., Muñoz-Sabater, J., Nicolas, J.,
667 Peubey, C., Radu, R., Schepers, D., Simmons, A., Soci, C., Abdalla, S., Abellan, X., Balsamo, G.,
668 Bechtold, P., Biavati, G., Bidlot, J., Bonavita, M., Chiara, G.D., Dahlgren, P., Dee, D., Diamantakis,
669 M., Dragani, R., Flemming, J., Forbes, R., Fuentes, M., Geer, A., Haimberger, L., Healy, S., Hogan,
670 R.J., Hólm, E., Janisková, M., Keeley, S., Laloyaux, P., Lopez, P., Lupu, C., Radnoti, G., Rosnay, P.
671 de, Rozum, I., Vamborg, F., Villaume, S., Thépaut, J.-N. The ERA5 global reanalysis. *Q. J. R.*
672 *Meteorol. Soc.* **2020**, 146, 1999–2049. <https://doi.org/10.1002/qj.3803>
- 673 (58) Boike, J., Juszak, I., Lange, S., Chadburn, S., Burke, E.J., Overduin, P.P., Roth, K., Ippisch, O.,
674 Bornemann, N., Stern, L., Gouttevin, I., Hauber, E., Westermann, S. Measurements in soil and air at
675 Bayelva Station. Supplement to: Boike, J et al. (2018): A 20-year record (1998-2017) of permafrost,
676 active layer and meteorological conditions at a high Arctic permafrost research site (Bayelva,
677 Spitsbergen). *Earth Syst. Sci. Data*, **2017**, 10, 355-390, <https://doi.org/10.5194/essd-10-355-2018>.
- 678 (59) EMEP. Manual for sampling and chemical analysis, Norwegian Institute for Air Research, Kjeller,
679 EMEP Report 1/95 (Last rev. 2001), <https://projects.nilu.no/ccc/manual/index.html> (last access: 12.
680 April 2021)
- 681 (60) Hirdman, D., Aspö, K., Burkhart, J.F., Eckhardt, S., Sodemann, H., Stohl, A. Transport of mercury
682 in the Arctic atmosphere: Evidence for a spring-time net sink and summer-time source. *Geophys.*
683 *Res. Lett.* **2009**, 36. <https://doi.org/10.1029/2009GL038345>
- 684 (61) Fisher, J.A., Jacob, D.J., Soerensen, A.L., Amos, H.M., Steffen, A., Sunderland, E.M. Riverine
685 source of Arctic Ocean mercury inferred from atmospheric observations. *Nat. Geosci.* **2012**, 5, 499–
686 504. <https://doi.org/10.1038/ngeo1478>
- 687 (62) Sonke, J.E., Teisserenc, R., Heimbürger-Boavida, L.-E., Petrova, M.V., Maruszczak, N., Dantec, T.L.,
688 Chupakov, A.V., Li, C., Thackray, C.P., Sunderland, E.M., Tananaev, N., Pokrovsky, O.S. Eurasian
689 river spring flood observations support net Arctic Ocean mercury export to the atmosphere and
690 Atlantic Ocean. *PNAS* **2018**, 115, E11586–E11594. <https://doi.org/10.1073/pnas.1811957115>
- 691 (63) Gustin, M.S., Dunham-Cheatham, S.M., Huang, J., Lindberg, S., Lyman, S.N. Development of an
692 Understanding of Reactive Mercury in Ambient Air: A Review. *Atmosphere* **2021b**, 12, 73.
693 <https://doi.org/10.3390/atmos12010073>
- 694 (64) Horowitz, H.M., Jacob, D.J., Zhang, Y., Dibble, T.S., Slemr, F., Amos, H.M., Schmidt, J.A., Corbitt,
695 E.S., Marais, E.A., Sunderland, E.M. A new mechanism for atmospheric mercury redox chemistry:
696 implications for the global mercury budget. *Atmos. Chem. Phys.* **2017**, 17, 6353–6371.
697 <https://doi.org/10.5194/acp-17-6353-2017>
- 698 (65) Peleg, M., Tas, E., Obrist, D., Matveev, V., Moore, C., Gabay, M., Luria, M. Observational Evidence
699 for Involvement of Nitrate Radicals in Nighttime Oxidation of Mercury. *Environ. Sci. Technol.* **2015**,
700 49, 14008–14018. <https://doi.org/10.1021/acs.est.5b03894>
- 701 (66) Jiao, Y. and Dibble, T.S. First kinetic study of the atmospherically important reactions $\text{BrHg}^+ + \text{NO}_2$

- 702 and $\text{BrHg}^{\cdot} + \text{HOO}$. *Phys. Chem. Chem. Phys.* **2017**, 19, 1826–1838.
703 <https://doi.org/10.1039/C6CP06276H>
- 704 (67) Lam, K.T., Wilhelmson, C.J., Schwid, A.C., Jiao, Y., Dibble, T.S. Computational Study on the
705 Photolysis of BrHgONO and the Reactions of BrHgO^{\cdot} with CH_4 , C_2H_6 , NO , and NO_2 : Implications
706 for Formation of Hg(II) Compounds in the Atmosphere. *J. Phys. Chem. A* **2019**, 123, 1637–1647.
707 <https://doi.org/10.1021/acs.jpca.8b11216>
- 708 (68) Dibble, T.S., Zelig, M.J., Mao, H. Thermodynamics of reactions of ClHg and BrHg radicals with
709 atmospherically abundant free radicals. *Atmos. Chem. Phys.* **2012**, 12, 10271–10279.
710 <https://doi.org/10.5194/acp-12-10271-2012>
- 711 (69) Toyota, K., McConnell, J.C., Lupu, A., Neary, L., McLinden, C.A., Richter, A., Kwok, R.,
712 Semeniuk, K., Kaminski, J.W., Gong, S.-L., Jarosz, J., Chipperfield, M.P., Sioris, C.E., 2011.
713 Analysis of reactive bromine production and ozone depletion in the Arctic boundary layer using 3-D
714 simulations with GEM-AQ: inference from synoptic-scale patterns. *Atmospheric Chemistry and*
715 *Physics* 11, 3949–3979. <https://doi.org/10.5194/acp-11-3949-2011>
- 716 (70) Yang, X., Pyle, J.A., Cox, R.A., 2008. Sea salt aerosol production and bromine release: Role of snow
717 on sea ice. *Geophysical Research Letters* 35. <https://doi.org/10.1029/2008GL034536>
- 718 (71) Huang, J., Jaeglé, L., Chen, Q., Alexander, B., Sherwen, T., Evans, M. J., Theys, N., and Choi, S.,
719 2020. Evaluating the impact of blowing snow sea salt aerosol on springtime BrO and O_3 in the
720 Arctic, *Atmos. Chem. Phys.*, 20, 7335–7358, <https://doi.org/10.5194/acp-20-7335-2020>.
- 721 (72) Simpson, W.R., Brown, S.S., Saiz-Lopez, A., Thornton, J.A., von Glasow, R. Tropospheric Halogen
722 Chemistry: Sources, Cycling, and Impacts. *Chem. Rev.* **2015**, 115, 4035–4062.
723 <https://doi.org/10.1021/cr5006638>
- 724 (73) Simpson, W.R., Glasow, R. von, Riedel, K., Anderson, P., Ariya, P., Bottenheim, J., Burrows, J.,
725 Carpenter, L.J., Friess, U., Goodsite, M.E., Heard, D., Hutterli, M., Jacobi, H.W., Kaleschke, L.,
726 Neff, B., Plane, J., Platt, U., Richter, A., Roscoe, H., Sander, R., Shepson, P., Sodeau, J., Steffen, A.,
727 Wagner, T., Wolff, E. Halogens and their role in polar boundary-layer ozone depletion. *Atmos.*
728 *Chem. Phys.* **2007**, 7, 4375–4418. <https://doi.org/10.5194/acp-7-4375-2007>
- 729 (74) Abbatt, J.P.D., Thomas, J.L., Abrahamsson, K., Boxe, C., Granfors, A., Jones, A.E., King, M.D.,
730 Saiz-Lopez, A., Shepson, P.B., Sodeau, J., Toohey, D.W., Toubin, C., von Glasow, R., Wren, S.N.,
731 Yang, X. Halogen activation via interactions with environmental ice and snow in the polar lower
732 troposphere and other regions. *Atmos. Chem. Phys.* **2012**, 12, 6237–6271.
733 <https://doi.org/10.5194/acp-12-6237-2012>
- 734 (75) Foster, K.L., Plastringe, R.A., Bottenheim, J.W., Shepson, P.B., Finlayson-Pitts, B.J., Spicer, C.W.
735 The Role of Br_2 and BrCl in Surface Ozone Destruction at Polar Sunrise. *Science* **2001**, 291, 471–
736 474. <https://doi.org/10.1126/science.291.5503.471>
- 737 (76) Liao, J., Huey, L.G., Liu, Z., Tanner, D.J., Cantrell, C.A., Orlando, J.J., Flocke, F.M., Shepson, P.B.,
738 Weinheimer, A.J., Hall, S.R., Ullmann, K., Beine, H.J., Wang, Y., Ingall, E.D., Stephens, C.R.,
739 Hornbrook, R.S., Apel, E.C., Riemer, D., Fried, A., Mauldin, R.L., Smith, J.N., Staebler, R.M.,

- 740 Neuman, J.A., Nowak, J.B. High levels of molecular chlorine in the Arctic atmosphere. *Nat. Geosci.*
741 **2014**, 7, 91–94. <https://doi.org/10.1038/ngeo2046>
- 742 (77) Zhang, L. and Jaffe, D.A. Trends and sources of ozone and sub-micron aerosols at the Mt. Bachelor
743 Observatory (MBO) during 2004-2015. *Atmospheric Environ.* **2017**, 165, 143–154.
744 <https://doi.org/10.1016/j.atmosenv.2017.06.042>
- 745 (78) Pal, B. and Ariya, P.A. Studies of ozone initiated reactions of gaseous mercury: kinetics, product
746 studies, and atmospheric implications. *Phys. Chem. Chem. Phys.* 2004, 6, 572–579.
747 <https://doi.org/10.1039/B311150D>
- 748 (79) Lyman, S. N., Gustin, M. S., Prestbo, E. M. A passive sampler for ambient gaseous oxidized mercury
749 concentrations. *Atmospheric Environ.* **2010**, 44, 246–252.
750 <https://doi.org/10.1016/j.atmosenv.2009.10.008>
- 751 (80) Huang, J., Lyman, S.N., Hartman, J.S., Gustin, M.S. A review of passive sampling systems for
752 ambient air mercury measurements. *Environ. Sci. Process Impacts* **2014**, 16, 374–392.
753 <https://doi.org/10.1039/c3em00501a>
- 754 (81) Huang, J. and Gustin, M.S. Uncertainties of Gaseous Oxidized Mercury Measurements Using KCl-
755 Coated Denuders, Cation-Exchange Membranes, and Nylon Membranes: Humidity Influences.
756 *Environ. Sci. Technol.* **2015**, 49, 6102–6108. <https://doi.org/10.1021/acs.est.5b00098>
- 757 (82) Sprovieri, F., Pirrone, N., Bencardino, M., D'Amore, F., Angot, H., Barbante, C., Brunke, E.-G.,
758 Arcega-Cabrera, F., Cairns, W., Comero, S., Diéguez, M.D.C., Dommergue, A., Ebinghaus, R.,
759 Feng, X.B., Fu, X., Garcia, P.E., Gawlik, B.M., Hageström, U., Hansson, K., Horvat, M., Kotnik, J.,
760 Labuschagne, C., Magand, O., Martin, L., Mashyanov, N., Mkololo, T., Munthe, J., Obolkin, V.,
761 Ramirez Islas, M., Sena, F., Somerset, V., Spandow, P., Vardè, M., Walters, C., Wängberg, I.,
762 Weigelt, A., Yang, X., Zhang, H. Five-year records of mercury wet deposition flux at GMOS sites in
763 the Northern and Southern hemispheres. *Atmos. Chem. Phys.* **2017**, 17, 2689–2708.
764 <https://doi.org/10.5194/acp-17-2689-2017>
- 765

766



TOC

767